Optical Flow Driven Interpolation for Isotropic FIB-SEM Reconstructions

V. González-Ruiz[a,*], J. P. García-Ortiz[a],
M. R. Fernández-Fernández[b], J. J. Fernández[b,*]

[a] *University of Almería, Ctra. Sacramento, s/n, Almería, 04120, Spain*
[b] *Spanish National Research Council (CINN-CSIC). Health Research Institute of Asturias (ISPA), Av Hospital Universitario s/n, Oviedo, 33011, Spain*

Abstract

Background and Objective: Focused Ion Beam - Scanning Electron Microscopy (FIB-SEM) allows three-dimensional ultrastructural analysis of cells and tissues at an isotropic resolution of a few nanometers. The technique iteratively removes a section of the sample with a FIB and takes an SEM image from the exposed surface. The section thickness is usually higher than the image pixel size to reduce acquisition time, thus resulting in anisotropic resolution. In this work, we explore novel interpolation methods along the sectioning direction to produce isotropic resolution and facilitate proper interpretation of the FIB-SEM 3D volumes.
Methods: Classical interpolation methods are usually applied in this context under the assumption that the changes through successive images are relatively smooth. However, the actual 3D arrangement of the structures in the sample may cause significant changes in the biological features between consecutive images of the FIB-SEM stacks. We have developed a novel interpolation strategy that accounts for this variation by using the Optical Flow (OF) to estimate it. Next, OF-compensated images are produced by aligning the spatial regions of the biological structures. The interpolation is finally applied to these OF-compensated images.
Results: Evaluation of the OF-driven and classical interpolation methods was carried out with a quantitative study based on Structural Similarity Index

---

[*] Corresponding authors:
Email addresses: `vruiz@ual.es` (V. González-Ruiz), `JJ.Fernandez@csic.es` (J. J. Fernández)

Measure (SSIM) and a qualitative evaluation based on visual results, using public datasets and representative anisotropy conditions. The quantitative evaluation demonstrated that the OF-driven interpolation always yields higher SSIM values, with interpolated images closer to the ground truth. The qualitative evaluation corroborated the quantitative results and confirmed that classical interpolation may blur areas with substantial changes between consecutive images whereas OF-driven interpolation succeeds in providing sharpness.

Conclusions: We have developed and evaluated an OF-driven interpolation approach to generating FIB-SEM stacks with isotropic resolution from experimental anisotropic data. Thanks to the OF, the interpolation adapts to the rapid variation of the biological structures observed through the images of the FIB-SEM stack. Our approach outperforms classical interpolation and manages to produce sharp interpolated views in cases where there are significant changes between consecutive experimental images.

Keywords: Interpolation, Optical Flow, FIB-SEM tomography, Anisotropy

1. Introduction

Large volume Electron Microscopy (EM) techniques allow the ultrastructural analysis of whole cells and tissues in three-dimensions (3D) at the nanoscale [1, 2]. They make it possible to study the cellular compartments and their interrelationships in their native spatial context. Thanks to the recent developments, these EM techniques have matured into essential tools in cell biology, biomedicine and health research.

FIB-SEM (Focused Ion Beam - Scanning Electron Microscopy) currently represents the finest of the large volume EM technologies. This technique proceeds in an automated fashion by iteratively removing an ultrathin section of the sample (as thin as 3-10 nm) with a FIB followed by imaging the freshly exposed surface with an SEM [3]. Afterward, the collected serial images are mutually aligned and stacked to produce a 3D volume (also known as FIB-SEM stack hereinafter) that is subjected to visualization and interpretation [1, 4].

FIB-SEM offers the highest resolution of the large volume EM technologies (up to 3-5 nm) and is the only one that can achieve isotropic resolution (i.e. section thickness equal to the image pixel size) [3]. Therefore, it has got a unique ability to visualize samples with a thickness of tens or hundreds of micrometers at an isotropic resolution of 3-5 nm. A number of recent breakthroughs in cell biology, neurobiology and biomedicine have made the most of FIB-SEM [5, 6, 7, 8, 9, 10].

Despite its potential, the FIB-SEM technique is limited by the slow operation of the current devices. This has a direct impact on the acquisition wall-time and cost, as well as in the instabilities of the imaging conditions and system reliability [3]. As a consequence, this factor inherently imposes a limitation in the depth of the sample that can be explored [3]. In practice, to image the sample as deep as possible in a reasonable time, the section thickness is set up to typically 2-4× the image pixel size, thus resulting in stacks with anisotropic resolution [9, 10, 11, 12] (for instance, image pixel size of 5 nm and section thickness of 20 nm). This anisotropy may hamper the proper interpretation of the 3D volumes.

Classical interpolation techniques (e.g. nearest neighbor, linear, cubic) are usually employed to overcome this anisotropy and thus produce FIB-SEM stacks with isotropic resolution, with linear interpolation being the standard method in the field [10]. Interpolation is applied along the Z direction (i.e. section thickness) to equal the resolution in X and Y directions (i.e. image pixel size). These classical methods are characterized by their simplicity and assume that the changes of structures in consecutive images are smooth. They thus neglect the rapid variation of the biological features and their position perpendicular to the sectioning direction, and this may produce interpolated images where some features appear blurred.

Recently, deep-learning-based super-resolution techniques have been explored in this context [13, 14, 15]. These works have demonstrated the need for sophisticated neuronal network architectures as well as proper image preprocessing and selection of training data for a successful application to the problem of anisotropy in FIB-SEM. Even so, the results obtained were similar to the classical methods [13, 14, 15]. Moreover, additional drawbacks are the high computational demands required by these approaches and the need for re-training the networks to be applied to FIB-SEM stacks acquired under different imaging settings or from different samples. As a consequence, these methods are not generally used at a practical level, and classical interpolation methods remain predominant in the FIB-SEM field and widespread in standard software packages (e.g. ImageJ, Fiji, DragonFly).

In this work, we introduce and evaluate a novel approach to interpolation of FIB-SEM stacks that is based upon Optical Flow (OF). OF is a classical technique to estimate the motion of objects between consecutive images of a sequence, with countless applications in video processing and computer vision [16]. Thanks to OF, our interpolation approach can adapt to the rapid variation of the biological structures between consecutive images of the stack, thereby outperforming the classical interpolation methods.

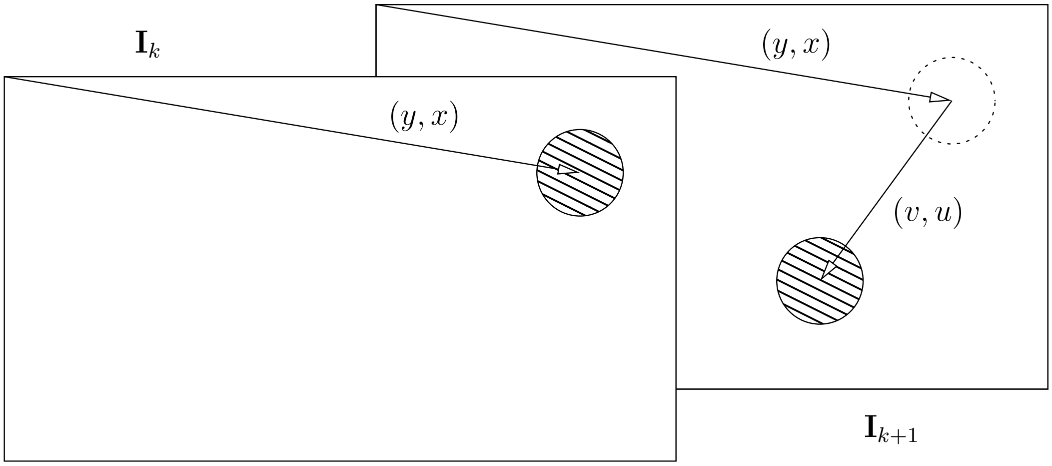

Figure 1: Definition context of the OF. The vector (v, u) connects a group of pixels associated to the same biological structure across the adjacent images $\mathbf{I}_k$ and $\mathbf{I}_{k+1}$.

2. Methods

2.1. Optical Flow definition

The concept of OF was conceived to describe the visual stimulus that allows animals to perceive movements in their surrounding environment. In the context of digital video, when a scene is captured at different times, moving (3D) objects are projected into groups of corresponding pixels in the (2D) images. In general, it is possible to estimate the displacement of the objects between consecutive frames/images, and this information is known as the OF [17]. In the FIB-SEM context, we aim to estimate the displacement of the 2D patterns generated by the 3D biological structures across the images of the stack.

In an ideal situation, pixels of adjacent images of the stack tend to satisfy the *intensity constancy assumption*: the values of the pixels related by the OF remain constant between the images. This (idealistic) behaviour has been described in Fig. 1 and is expressed by

$$\mathbf{I}_{k+1,y+v,x+u} = \mathbf{I}_{k,y,x} \tag{1}$$

where $\mathbf{I}$ is a stack, $\mathbf{I}_k$ is the k-th image of $\mathbf{I}$, $\mathbf{I}_{k,y,x}$ is the intensity of the pixel with coordinates (y, x) of $\mathbf{I}_k$ and (v, u) is the vector that relates (connects) the pixels projected by the same structure between the images.

In general, the objective is to find (v, u) that minimizes

$$\mathbf{E}_{y,x} = s\big(\mathbf{I}_{k+1,y+v,x+u}, \mathbf{I}_{k,y,x}\big), \tag{2}$$

where $s(\cdot, \cdot)$ is a function that measures similarity between pixels [17]. For example, if we minimize the squared error, we use

$$\mathbf{E}_{y,x} = ||\mathbf{I}_{k+1,y+v,x+u} - \mathbf{I}_{k,y,x}||^2, \tag{3}$$

or even better, considering a neighborhood defined by a window $\mathbf{W}$

$$\mathbf{E}_{y,x} = \sum_{(y',x')\in\mathbf{W}} ||\mathbf{I}_{k+1,y'+v,x'+u} - \mathbf{I}_{k,y',x'}||^2, \tag{4}$$

increasing the robustness to noise but also decreasing the structural accuracy of the OF field, by introducing an implicit smoothing factor that depends on the size and the shape of $\mathbf{W}$.

Unfortunately, we cannot determine (v, u) using only one equation (there are many possible pairs of values for u and v that satisfy Eq. 4). This issue is known as the *aperture problem* and makes the OF computation ill-posed [17]. For this reason, the different OF estimators that have been developed use some extra constraints to address this problem.

2.2. Farnebäck OF estimator

The Farnebäck's estimator [18] minimizes Eq. 4 in a quadratic polynomial domain, where each pixel's neighborhood is modeled by a quadratic function

$$f(\mathbf{x}) = \mathbf{x}^\intercal\mathbf{A}\mathbf{x} + \mathbf{b}^\intercal\mathbf{x} + c, \tag{5}$$

where $\mathbf{x} = (y, x)$ is the pixel, $\cdot^\intercal$ represents the transpose of a vector or a matrix, $\mathbf{A}$ is a (symmetric) matrix, $\mathbf{b}$ a vector, and c a scalar. The polynomial coefficients $\mathbf{A}$, $\mathbf{b}$ and c are estimated in terms of normalized convolution [19] with the basis functions

$$\{1, x, y, x^2, y^2, xy\}, \tag{6}$$

obtaining

$$f(\mathbf{x}) = r_1 + r_2 x + r_3 y + r_4 x^2 + r_5 y^2 + r_6 xy \tag{7}$$

that is related to Eq. 5 as

$$c = r_1, \mathbf{b} = \begin{bmatrix} r_2 \\ r_3 \end{bmatrix}, \text{ and } \mathbf{A} = \begin{bmatrix} r_4 & r_6/2 \\ r_6/2 & r_5 \end{bmatrix}. \tag{8}$$

The size of the sampled convolution kernels (the so-called *applicability* that usually is a Gaussian filter [18]) determines the scale of the structures captured by the polynomial expansion. In such domain, if we have

$$f_1(\mathbf{x}) = \mathbf{x}^\intercal \mathbf{A}_1 \mathbf{x} + \mathbf{b}_1{}^\intercal \mathbf{x} + c_1, \tag{9}$$

and assume a new signal

$$f_2(\mathbf{x}) = \mathbf{x}^\intercal \mathbf{A}_2 \mathbf{x} + \mathbf{b}_2{}^\intercal \mathbf{x} + c_2, \tag{10}$$

resulting of a global displacement $\mathbf{d}$ with respect to f_1

$$\begin{aligned} f_2(\mathbf{x}) &= f_1(\mathbf{x} - \mathbf{d}) \\ &= (\mathbf{x} - \mathbf{d})^\intercal \mathbf{A}_1 (\mathbf{x} - \mathbf{d}) + \mathbf{b}_1{}^\intercal (\mathbf{x} - \mathbf{d}) + c_1 \\ &= \mathbf{x}^\intercal \mathbf{A}_1 \mathbf{x} + (\mathbf{b}_1 - 2\mathbf{A}_1 \mathbf{d})^\intercal \mathbf{x} + \mathbf{d}^\intercal \mathbf{A}_1 \mathbf{d} + \mathbf{b}_1{}^\intercal \mathbf{d} + c_1, \end{aligned} \tag{11}$$

then we obtain that [18]

$$\mathbf{A}_2 = \mathbf{A}_1, \tag{12}$$

$$\mathbf{b}_2 = \mathbf{b}_1 - 2\mathbf{A}_1 \mathbf{d}, \tag{13}$$

$$c_2 = \mathbf{d}^\intercal \mathbf{A}_1 \mathbf{d} - \mathbf{b}_1{}^\intercal \mathbf{d} + c_1. \tag{14}$$

The displacement $\mathbf{d}$ can be determined by Eq. 13, provided that $\mathbf{A}_1$ is non-singular, using [18]

$$\mathbf{d} = -\frac{1}{2} \mathbf{A}_1{}^{-1} (\mathbf{b}_2 - \mathbf{b}_1). \tag{15}$$

Since a whole image is unlikely to be modeled by a single polynomial and the displacement is expected to vary spatially across the image, the derivation requires to be further elaborated. For this reason, the global polynomials in Eqs. 9 and 10 are replaced by local polynomial approximations, thus obtaining [18]

$$f_1(\mathbf{x}) = \mathbf{x}^\intercal \mathbf{A}_1(\mathbf{x}) \mathbf{x} + \mathbf{b}_1{}^\intercal (\mathbf{x}) \mathbf{x} + c_1 \tag{16}$$

and

$$f_2(\mathbf{x}) = \mathbf{x}^\intercal \mathbf{A}_2(\mathbf{x})\mathbf{x} + \mathbf{b}_2{}^\intercal(\mathbf{x})\mathbf{x} + c_2. \tag{17}$$

As we can see in Eq. 12, $\mathbf{A}_2(\mathbf{x}) = \mathbf{A}_1(\mathbf{x})$, but in practice these matrices are only similar, and it is more robust (against noise) to use

$$\mathbf{A}(\mathbf{x}) = \frac{\mathbf{A}_1(\mathbf{x}) + \mathbf{A}_2(\mathbf{x})}{2}. \tag{18}$$

Now, if we introduce

$$\Delta\mathbf{b}(\mathbf{x}) = -\frac{1}{2}\big(\mathbf{b}_2(\mathbf{x}) - \mathbf{b}_1(\mathbf{x})\big), \tag{19}$$

then, using Eq. 13, we obtain the primary constraint

$$\mathbf{A}(\mathbf{x})\mathbf{d}(\mathbf{x}) = \Delta\mathbf{b}(\mathbf{x}), \tag{20}$$

where $\mathbf{d}(\mathbf{x})$ is a spatially varying displacement field. Notice that Eqs. 1 and 20 are equivalent (relates the same information but in different domains) and therefore, we still have an undetermined system with two unknowns ($\mathbf{d}(\mathbf{x})$) and only one equation. To solve this, let us assume now that the displacement field in Eq. 20 is slowly varying (the so-called *motion smoothness assumption* used in most OF estimators) and consider a neighborhood defined by a window $\mathbf{W}$, thus introducing an implicit smoothing factor and making the algorithm more robust to noise. Now we minimize

$$\sum_{\Delta\mathbf{x}\in\mathbf{W}} w(\Delta\mathbf{x})||\mathbf{A}(\mathbf{x}+\Delta\mathbf{x})\mathbf{d}(\mathbf{x}) - \Delta\mathbf{b}(\mathbf{x}+\Delta\mathbf{x})||^2, \tag{21}$$

where $\Delta\mathbf{x}$ denotes the neighborhood of $\mathbf{x}$ and $w(\Delta\mathbf{x})$ describes the applicability, typically a 2D Gaussian function covering the neighborhood window $\mathbf{W}$. The minimum is obtained for

$$\mathbf{d}(\mathbf{x}) = \Big(\sum_{\Delta\mathbf{x}\in\mathbf{W}} w(\Delta\mathbf{x})\mathbf{A}^\intercal\mathbf{A}\Big)^{-1} \sum_{\Delta\mathbf{x}\in\mathbf{W}} w(\Delta\mathbf{x})\mathbf{A}^\intercal\Delta\mathbf{b}, \tag{22}$$

or by simplifying the notation

$$\mathbf{d}(\mathbf{x}) = \Big(\sum_{\Delta\mathbf{x}\in\mathbf{W}} w\mathbf{A}^\intercal\mathbf{A}\Big)^{-1} \sum_{\Delta\mathbf{x}\in\mathbf{W}} w\mathbf{A}^\intercal\Delta\mathbf{b}. \tag{23}$$

At this point, we can still improve the robustness if the displacement field is parameterized according to the quadratic motion model [18]:

$$\begin{aligned} d_x(y,x) &= a_1 + a_2x + a_3y + a_7x^2 + a_8xy, \\ d_y(y,x) &= a_4 + a_5x + a_6y + a_7xy + a_8y^2, \end{aligned} \tag{24}$$

that can be written in matrix form as

$$\mathbf{d} = \mathbf{S}\mathbf{p}, \tag{25}$$

where

$$\mathbf{S} = \begin{bmatrix} 1 & x & y & 0 & 0 & 0 & x^2 & xy \\ 0 & 0 & 0 & 1 & x & y & xy & y^2 \end{bmatrix}, \tag{26}$$

and

$$\mathbf{p} = \begin{bmatrix} a_1 & a_2 & a_3 & a_4 & a_5 & a_6 & a_7 & a_8 \end{bmatrix}^\intercal. \tag{27}$$

Substituting in Eq. 21, we obtain the weighted least squares problem

$$\sum_i w_i ||\mathbf{A}_i\mathbf{S}_i\mathbf{p} - \Delta\mathbf{b}_i||^2, \tag{28}$$

where i indexes the coordinates in a neighborhood. The solution turns out to be [18]

$$\mathbf{p} = \left(\sum_i w_i {\mathbf{S}_i}^\intercal {\mathbf{A}_i}^\intercal \mathbf{A}_i \mathbf{S}_i\right)^{-1} \sum_i w_i {\mathbf{S}_i}^\intercal {\mathbf{A}_i}^\intercal \Delta\mathbf{b}_i. \tag{29}$$

Therefore, the Farnebäck estimator reduces to Eqs. 25, 26 and 29.

Practical implementations of the Farnebäck estimator involve multi-scale estimation of the OF [18], as we have used in this work, by using an approach similar to the Gaussian pyramid [20]. The method obtains an initial estimate of the displacement field by working at a coarse scale. The displacement estimate is then propagated through finer scales to progressively refine the estimates and increase the accuracy. The multi-scale implementation makes use of the estimated displacement field at the present scale, $\tilde{\mathbf{d}}(\mathbf{x})$, as a priori displacement in the next scale by replacing Eqs. 18 and 19 by

$$\mathbf{A}(\mathbf{x}) = \frac{\mathbf{A}_1(\mathbf{x}) + \mathbf{A}_2(\tilde{\mathbf{x}})}{2} \tag{30}$$

and

$$\Delta\mathbf{b}(\mathbf{x}) = -\frac{1}{2}\big(\mathbf{b}_2(\tilde{\mathbf{x}}) - \mathbf{b}_1(\mathbf{x})\big) + \mathbf{A}(\mathbf{x})\tilde{\mathbf{d}}(\mathbf{x}), \tag{31}$$

where

$$\tilde{\mathbf{x}} = \mathbf{x} + \tilde{\mathbf{d}}(\mathbf{x}). \tag{32}$$

The basic parameters of the Farnebäck OF estimator are the scale levels involved in the multi-scale implementation and the size of the neighborhood window $\mathbf{W}$. The former is related to the search area and the magnitude of displacements. The use of coarser scales allows the algorithm to handle large displacements but with potential risk of decreasing the accuracy. The latter is related to the noise and the size of the biological structures of interest. The larger the window size, the more robust the algorithm is against noise, but at the expense of structural accuracy if the window does not properly fit the size of the biological structures.

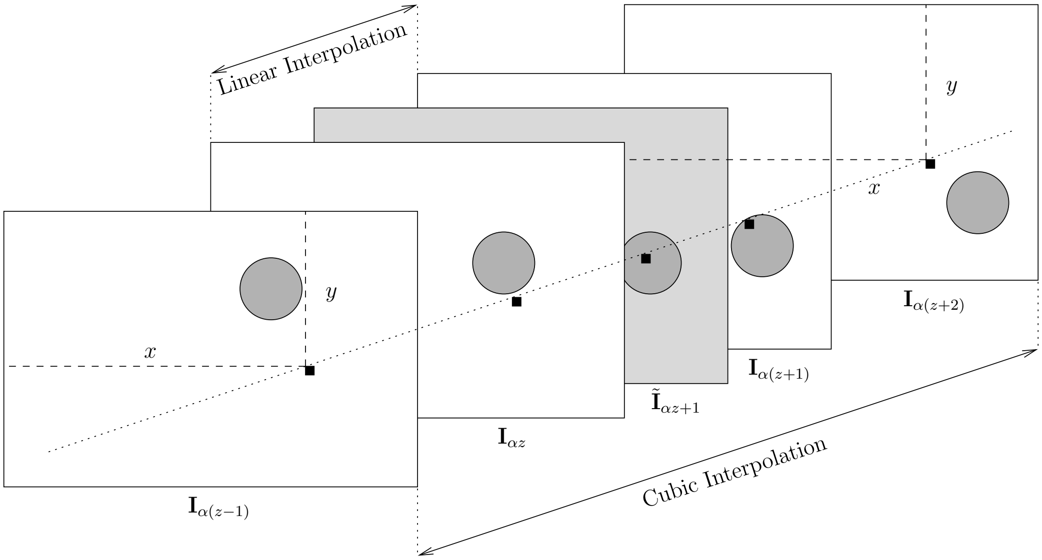

Figure 2: Linear and cubic interpolation without OF ($\alpha = 2$). Interpolation is carried out along the Z-axis (dotted line) ignoring the potential variation in location of the biological structures (grey circles).

2.3. Linear and cubic interpolation (without OF)

Given a set of known knots (evenly spaced points), interpolation is the task of finding an arbitrary continuously defined function that crosses through the knots and that exhibits some required properties, such as smoothness [21]. A way of building such function is through a discrete sum of weighted and shifted functions derived from a basis (interpolation kernel) $w(\cdot)$, performing a low pass filtering (and therefore, a discrete convolution between the knots and the sampled version of the basis) applied to the knots [22].

The kernel of linear interpolation is defined by

$$w^{\text{linear}}(x) = \begin{cases} 1 - x & \text{if } |x| < 1, \\ 0 & \text{otherwise,} \end{cases} \tag{33}$$

while cubic interpolation is determined by the piece-wise polynomial

$$w^{\text{cubic}}(x, a) = \begin{cases} (2-a)|x|^3 + (a-3)|x|^2 + 1 & \text{if } |x| < 1, \\ -a|x|^3 + 5a|x|^2 - 8a|x| + 4a & \text{if } 1 \leq |x| < 2, \\ 0 & \text{otherwise,} \end{cases} \tag{34}$$

that can be classified as a spline function, where $x \in \mathbb{R}$ represents the signed distance between the reference knot and the interpolated point, and the parameter a adjusts the steepness of the spline. In all our experiments $a = 1/2$ (configuring a Catmull-Rom spline [21]) to get a trade-off between smoothness and sharpness in the interpolations [23]. Therefore, we define

$$w(x) = w_{\mathrm{CR}}^{\mathrm{cubic}}(x) = w^{\mathrm{cubic}}(x, 1/2). \tag{35}$$

In the case of conventional linear interpolation (i.e. without OF) the selected image-knots (see Fig. 2) are $\{\mathbf{I}_{\alpha(z+i)}$ for $i = 0, 1\}$, where $\mathbf{I}$ is the anisotropic stack, $\alpha \in \mathbb{N}$ is the interpolation step size, and $z \in \mathbb{N}$ is the index of the image in $\mathbf{I}$, but considering consecutive indexes. For cubic interpolation, the set of image-knots becomes $\{\mathbf{I}_{\alpha(z+i)}$ for $i = -1, 0, 1, 2\}$.

Considering Eqs. 33 and 34 and the reference image-knots, the interpolated images are then calculated, with linear and cubic interpolation respectively, as:

$$\tilde{\mathbf{I}}_{\alpha z+j}^{\mathrm{linear}} = (1 - \beta_0)\mathbf{I}_{\alpha z} + \beta_0 \mathbf{I}_{\alpha(z+1)} \tag{36}$$

and

$$\tilde{\mathbf{I}}_{\alpha z+j}^{\mathrm{cubic}} = \textstyle\sum_{i=-1}^{2} w(\beta_i)\mathbf{I}_{\alpha(z+i)}, \tag{37}$$

with j=1, . . . , $(\alpha - 1)$, and where

$$\beta_i = \frac{(\alpha z + j) - \alpha(z + i)}{\alpha} = \frac{j - \alpha i}{\alpha}. \tag{38}$$

Notice that in the case of the cubic interpolation, the term $w(\beta_i)$ can be recognized as the contribution (to the interpolated image) of the i-th image indexed in the corresponding image-knots set. In the linear interpolation, the contributions have been directly expressed in terms of β_0 by “hard-coding” Eq. 33 into Eq. 36.

Finally, we want to highlight that because we are interpolating (not performing a regression), it holds that

$$\tilde{\mathbf{I}}_{\alpha z} = \mathbf{I}_{\alpha z}, \tag{39}$$

i.e., all the images of the anisotropic stack ($\mathbf{I}$) are part of the isotropic one ($\tilde{\mathbf{I}}$), and in between of each pair of those images with indexes αz and $\alpha(z+1)$,

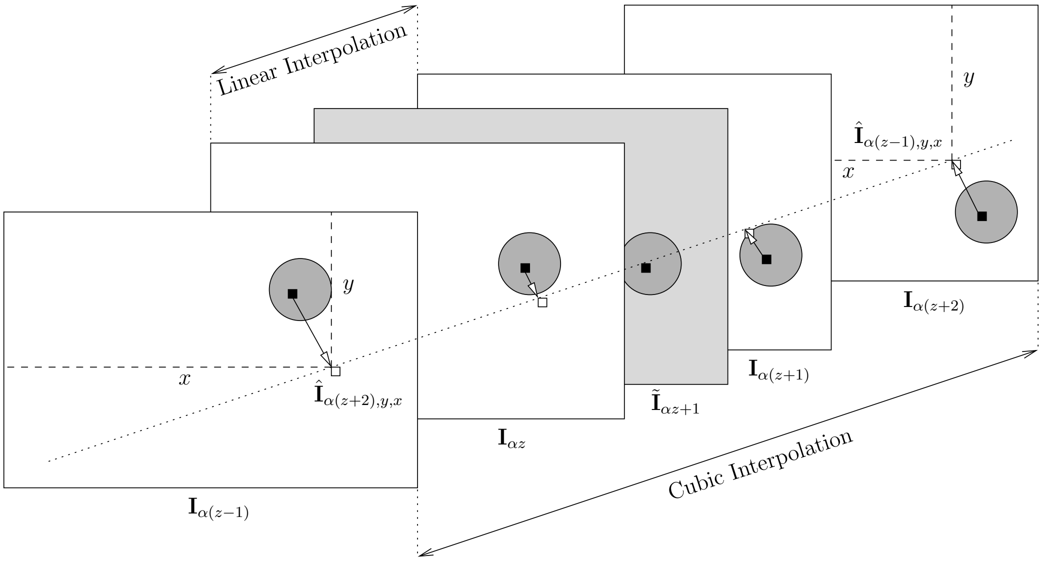

Figure 3: Linear and cubic interpolation with OF ($\alpha = 2$). In essence, images are transformed according to the estimated OF (arrows) to compensate for the variation in location undergone by the biological structures (grey circles), followed by interpolation along the Z-axis (dotted line).

a total of $\alpha - 1$ interpolated images are computed with (isotropic-domain) indexes $\alpha z + 1, \alpha z + 2, \ldots, \alpha(z + 1) - 1$. This idea has been shown in Fig. 2 where for simplicity $\alpha = 2$ and therefore, there exists only one interpolated image in the middle plane between each possible pair of original ones.

2.4. OF-driven linear and OF-driven cubic interpolation

Most biological structures present in the FIB-SEM stacks produce highly correlated patterns in neighboring images. These patterns change slightly their position across the XY plane through the images of the stack, according to the real 3D arrangement of the biological structures in the sample. If these variations in the positions of the patterns are not taken into consideration during the interpolation, the resulting images may turn out to be blurred. Fig. 2 illustrates the interpolation of image $\tilde{\mathbf{I}}_{\alpha z+1}$ from the corresponding image-knots. The small black square in that image denotes a specific pixel that belongs to the pattern associated with a particular biological structure (represented by a grey circle) that should appear, for example, at the $\alpha z + 1$

position of the Z-axis. Conventional interpolation, either linear or cubic as described in the previous section, ignores the variation of the position of that structure through the image-knots. The pixels involved in this interpolation are indicated by the dotted line running along the Z-axis. As a result, the biological structure will appear blurred in the interpolated image $\tilde{\mathbf{I}}_{\alpha z+1}$.

We have developed a new strategy to improve the interpolation of FIB-SEM stacks. The method consists of estimating the apparent motion undergone by the biological structures through adjacent images of the stack, followed by the alignment of the spatial regions of such structures so as to produce OF-compensated image-knots. Afterward, interpolation is applied as described in the previous section to produce the interpolated images of the isotropic stack from the corresponding knots. Therefore, we rely on OF to estimate the displacement of the structures and conduct the alignment that compensates for it. Fig. 3 illustrates our approach. Each original image-knot is transformed according to the estimated OF, so the spatial regions corresponding to specific biological structures are brought in register (denoted by the arrows). As a result, the interpolation along the Z-axis (represented by the dotted line) ensures the involvement of the proper pixels so as to improve the quality of the interpolated images and attenuate potential blurring.

We have used Farnebäck's algorithm described in Section 2.2 to compute the displacement field $\mathbf{d}(\mathbf{x})$ (or simply $\mathbf{d}$ in the rest of this section, see Eqs. 23 and 25) between the images in the anisotropic stack $\mathbf{I}$. The reason is because it offers excellent results [18], requires modest computational resources, and it is already implemented in OpenCV[1], though several other alternatives for dense OF exist (such as Dense Pyramid Lucas-Kanade [24] or PCA-Flow [25]).

Specifically, our OF-driven linear and cubic interpolations can be mathematically expressed as

$$\tilde{\mathbf{I}}_{\alpha z+j}^{\text{linear OF}} = (1-\beta_0)\hat{\mathbf{I}}_{\alpha(z+1)} + \beta_0\hat{\mathbf{I}}_{\alpha z} \tag{40}$$

---

[1] `https://docs.opencv.org/4.5.3/de/d9e/classcv_1_1FarnebackOpticalFlow.html`

and

$$\tilde{\mathbf{I}}_{\alpha z+j}^{\text{cubic OF}} = \textstyle\sum_{i=2}^{-1} w(\beta_{1-i})\hat{\mathbf{I}}_{\alpha(z+i)}, \tag{41}$$

where β_i and $w(\beta_i)$ were defined in the previous section.

It can be noticed that these equations are derived from the conventional interpolation, Eqs. 36 and 37, with the important difference that they are applied to the OF-compensated image-knots

$$\begin{aligned}
\hat{\mathbf{I}}_{\alpha(z-1)} &= \big((\tfrac{|\beta_2|}{3} \overset{\alpha(z+2)\to\alpha(z-1)}{\mathbf{d}})(\mathbf{I}_{\alpha(z+2)})\big), \\
\hat{\mathbf{I}}_{\alpha z} &= (|\beta_1| \overset{\alpha(z+1)\to\alpha z}{\mathbf{d}})(\mathbf{I}_{\alpha(z+1)}), \\
\hat{\mathbf{I}}_{\alpha(z+1)} &= (|\beta_0| \overset{\alpha z\to\alpha(z+1)}{\mathbf{d}})(\mathbf{I}_{\alpha z}), \\
\hat{\mathbf{I}}_{\alpha(z+2)} &= \big((\tfrac{|\beta_{-1}|}{3} \overset{\alpha(z-1)\to\alpha(z+2)}{\mathbf{d}})(\mathbf{I}_{\alpha(z-1)})\big),
\end{aligned} \tag{42}$$

where $\hat{\mathbf{I}}_i$ is the OF-compensated version of the original k-th image-knot $\mathbf{I}_k$ after transformation with the corresponding (scaled) displacement field $\overset{k\to i}{\mathbf{d}}$. The displacement fields are scaled (see factors $\frac{|\beta_{.}|}{3}$ or $|\beta_{.}|$ in Eq. 42) in order to generate the OF-compensated image-knots according to the distances between such images and the interpolated one with index $(\alpha z+j)$ (see Fig. 3).

3. Results

3.1. Quantitative Evaluation

3.1.1. Datasets and metric for the evaluation

To conduct the quantitative evaluation we used two public datasets from different samples and acquired under different imaging settings. First, we used a stack from the CA1 hippocampus region from rat brain acquired with a Zeiss NVision 40 FIB-SEM microscope using an isotropic pixel size of 5 nm (i.e., section thickness and image pixel spacing of 5 nm) [26]. The dataset is often used to assess automated segmentation methods [27] and is publicly available[2]. The second dataset was a stack from a worm *Platynereis dumerilii*, an animal typically used as a model organism in cell biology laboratories, acquired with a Zeiss Crossbeam 540 FIB-SEM microscope using an isotropic pixel size of 10 nm [28]. The dataset is deposited at the Electron Microscopy Public Image Archive (EMPIAR) [29] and accessible with ID 10310[3]. These original datasets are massive in size (nearly 2000 images). To reduce the computation costs and be able to assess the quality for individual images, the evaluation was restricted to substacks of 150 images. These datasets are denoted by EPFL and EMPIAR-10310, respectively, hereinafter.

The evaluation of the interpolation methods was carried out as follows. First, anisotropic acquisition conditions were simulated by subsampling the stacks in the Z direction. Three anisotropy conditions were tested: section thickness equal to 2×, 4× and 8× the image pixel size. The subsampling then consisted in taking images from the original stacks at steps of $\alpha = 2$, 4 and 8, respectively (i.e. taking one of every 2, 4 and 8 images, respectively), which acted as reference image-knots. Second, the interpolation methods were applied to the simulated anisotropic stacks in order to generate the missing images and thus produce isotropic stacks. Finally, the interpolated images were compared with the real images acting as ground truth.

The quantitative assessment was performed using the Structural Similar-

---

[2] `https://www.epfl.ch/labs/cvlab/data/data-em`

[3] `https://www.ebi.ac.uk/empiar/EMPIAR-10310`

ity Index Measure (SSIM) to compare the interpolated images with the real ones. The SSIM is a widespread metric that measures the similarity between two images based on structural information and by considering the pixel interrelationships in local regions [30]. The procedure sweeps a sliding window over the image space to confine the calculation of the SSIM metric to the local neighborhood. As a result, a SSIM map is obtained that describes the similarity across the image space. A single overall SSIM index of the whole image is then obtained by averaging the local SSIMs. SSIM values range from -1 to 1, with 1 indicating a perfect match.

The evaluation included the two OF-driven interpolation methods presented in this article, namely linear OF and cubic OF. For comparison, standard strategies that rely on classical linear and cubic interpolation were also included. The four methods were applied to the two datasets under the three anisotropy conditions (steps of $\alpha = 2$, 4 and 8 along the Z direction).

To tune the Farnebäck OF estimator, we conducted a series of tests and determined the parameters that were valid for all datasets. Specifically, we used three scale levels for the multi-scale OF approach and a neighborhood window of 129×129 pixels.

3.1.2. Results from the quantitative evaluation

Figures 4 and 5 show the SSIM values obtained for the individual interpolated images of the two tested datasets, EPFL and EMPIAR-10310, respectively. SSIM curves exhibit higher values at lower steps (i.e. smaller anisotropy, with a closer distance between the images serving as reference knots). Therefore, green ($\alpha = 2$), red ($\alpha = 4$) and blue ($\alpha = 8$) curves obtained using a specific interpolation method show decreasing SSIM values. The plots clearly demonstrate that OF-driven interpolation methods (presented with solid curves) significantly improve the quality of the interpolated images compared to the classical ones (dotted curves). The increase in SSIM is similar regardless of the interpolation strategy, either linear (top panels in the figures) or cubic (bottom panels). It is a remarkable fact that OF-driven interpolation at higher steps may approach, or even outperform, the classical methods at lower steps. This effect is seen, for instance, in Fig. 4 with OF-driven methods applied at step $\alpha = 4$ (solid red curve) outperforming

	EPFL			EMPIAR-10310		
	$\alpha = 2$	$\alpha = 4$	$\alpha = 8$	$\alpha = 2$	$\alpha = 4$	$\alpha = 8$
	10 nm	20 nm	40 nm	20 nm	40 nm	80 nm
linear	0.5948	0.5570	0.4705	0.5627	0.4951	0.3731
cubic	0.5829	0.5508	0.4714	0.5567	0.4950	0.3750
linear OF	**0.6323**	0.6030	0.5176	0.5839	0.5182	0.3944
cubic OF	0.6275	**0.6033**	**0.5225**	**0.5853**	**0.5232**	**0.3988**

Table 1: Average SSIM values.

classical ones at $\alpha = 2$ (dotted green curve).

Figures 4 and 5 also show that the SSIM values tend to vary slightly across the images of the FIB-SEM stack when the anisotropy is relatively low (e.g. step of $\alpha = 2$). However, this behavior changes for larger steps and significant oscillations can be observed at $\alpha = 8$, where local SSIM valleys are found at the halfway point between consecutive reference images. In these situations, OF does not manage to attenuate the oscillations but the overall improvement is still notable as the whole SSIM curve is raised throughout the entire range.

Table 1 presents the global SSIM values calculated by averaging the individual SSIM values in Figs. 4 and 5. The columns of the table label the anisotropy conditions ($\alpha = 2, 4, 8$) and, for completeness, the distance between the knots in the biological sample (in nm) is also included. This table summarizes the overall behavior observed in Figs. 4 and 5, further substantiating the superiority of OF-driven interpolation methods with respect to the corresponding classical ones, either linear or cubic. For instance, at step $\alpha = 4$, classical interpolations produce SSIMs around 0.55 and 0.49 for EPFL and EMPIAR-10310 datasets, respectively, whereas their OF-driven versions improve them to around 0.60 and 0.52. Moreover, this table also corroborates that (either classical or OF-driven) both linear and cubic interpolation behave similarly, with linear somewhat better than cubic at lower steps.

Figures 6 and 7 visually illustrate the benefits of using OF-driven interpolation methods on the two tested datasets. Isotropic stacks were constructed by assembling the interpolated images together with the reference knots. Those figures present two selected areas of the isotropic stacks and compare

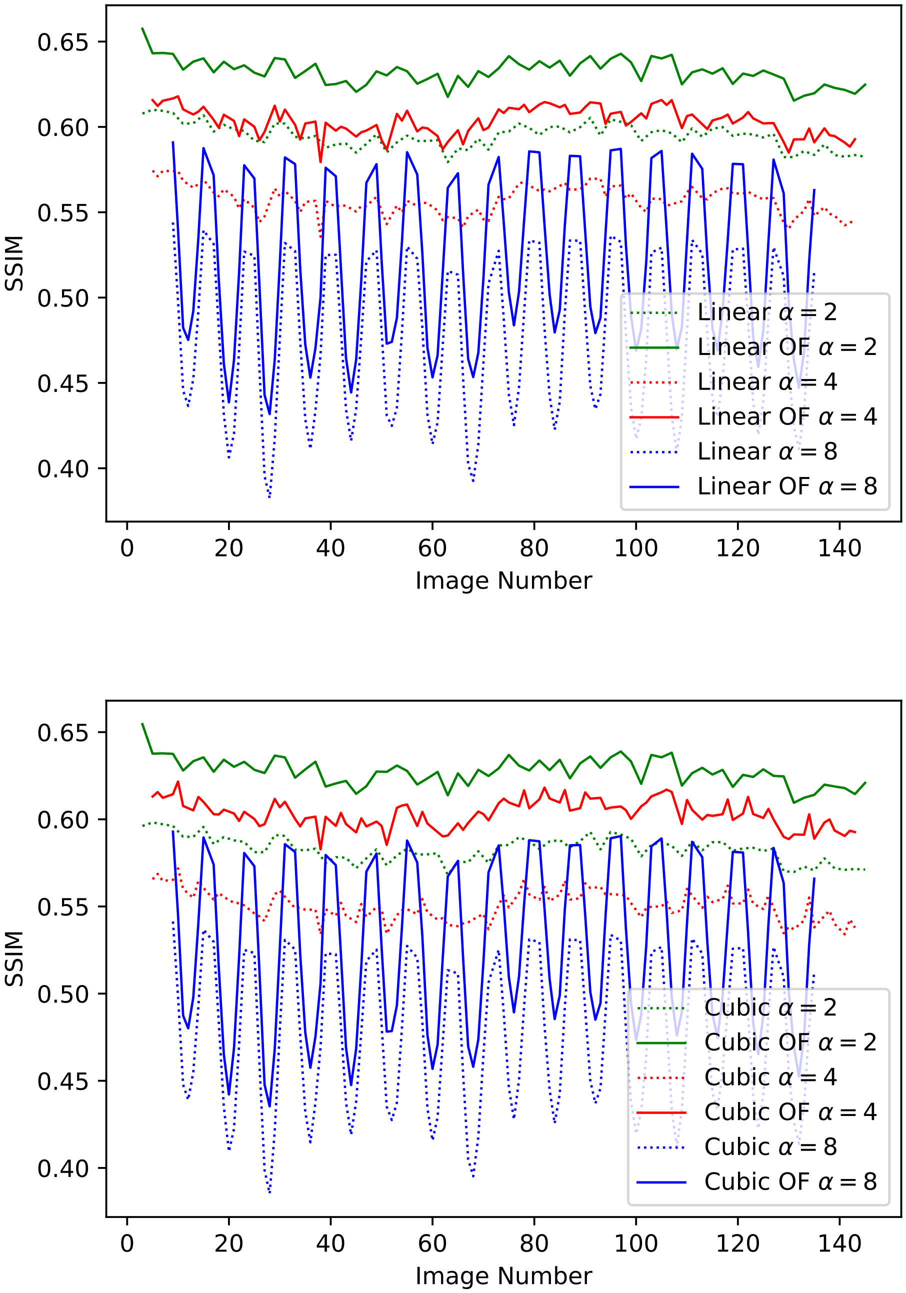

Figure 4: SSIM curves obtained from EPFL dataset.

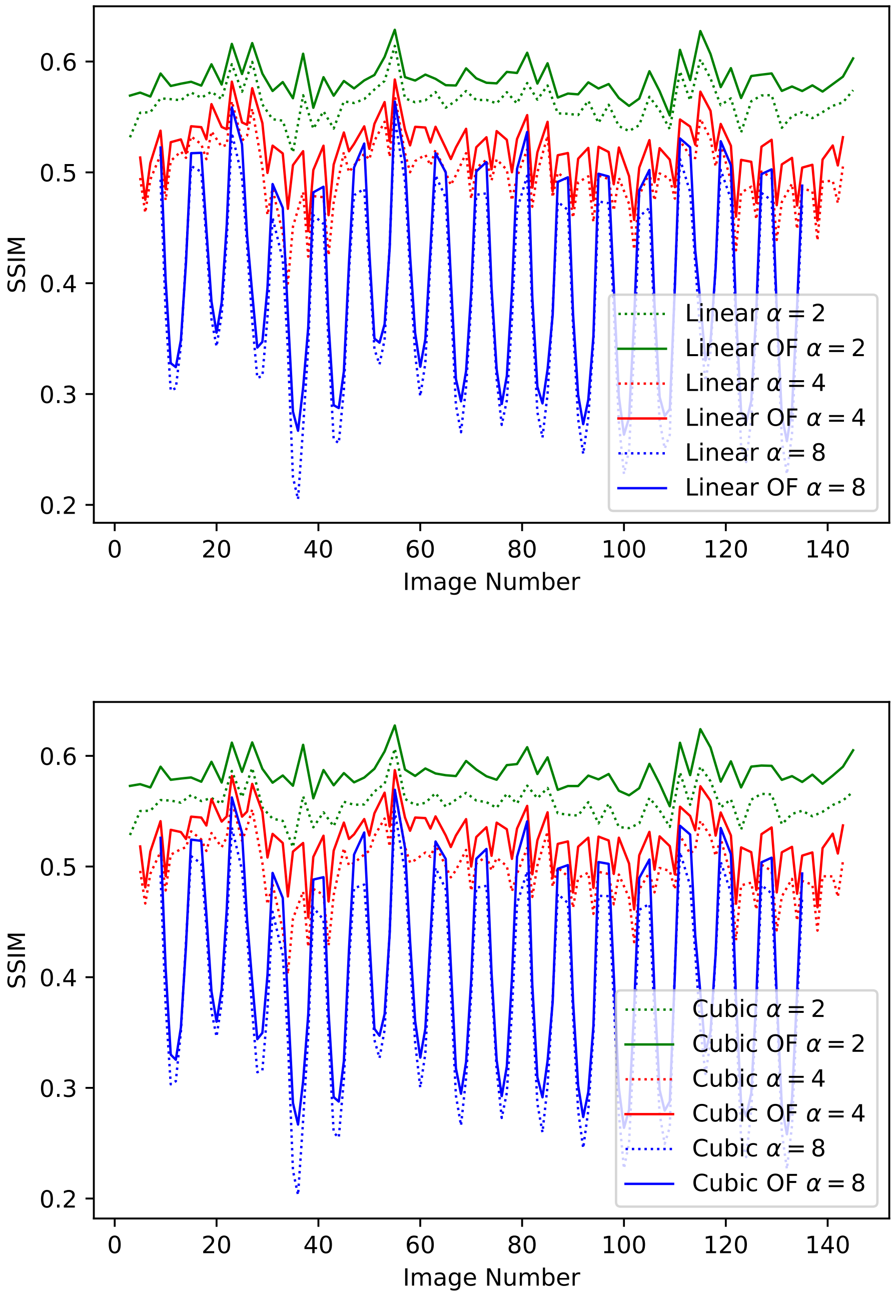

Figure 5: SSIM curves obtained from EMPIAR-10310 dataset.

them to the original stacks. For conciseness, only the results obtained under the anisotropy condition of $\alpha = 4$ are presented. Regions of particular interest are marked with arrows. The figures clearly show that features that rapidly vary along the Z-direction (i.e. the sectioning direction) are the most benefited from the OF-driven interpolation. Thus, the effects are especially noticeable at membranous structures running in diagonal in the XZ planes, as pointed by arrows in the figures. In these situations, classical interpolation, either linear or cubic, may produce apparent stair-like effects in the XZ planes (Figs. 6 and 7) and may exhibit significant blurring (see Fig. 7) in the interpolated images. In contrast, OF-driven methods produce sharp results, with interpolated images approaching the original ones and better XZ planes in the resulting isotropic stack. These figures also demonstrate from a visual point of view that there is a negligible difference between linear and cubic interpolation (either classical or considering OF).

Figure 8 presents SSIM maps corresponding to the images from which the areas in Fig. 6(top) and Fig. 7(top) were selected. These maps indicate that high SSIM values come from biological features that stand out from the background, such as membranes, and suggest that these features play an important role in guiding the OF-driven methods. Notice that these methods exhibit high SSIM values at the membranes and their edges.

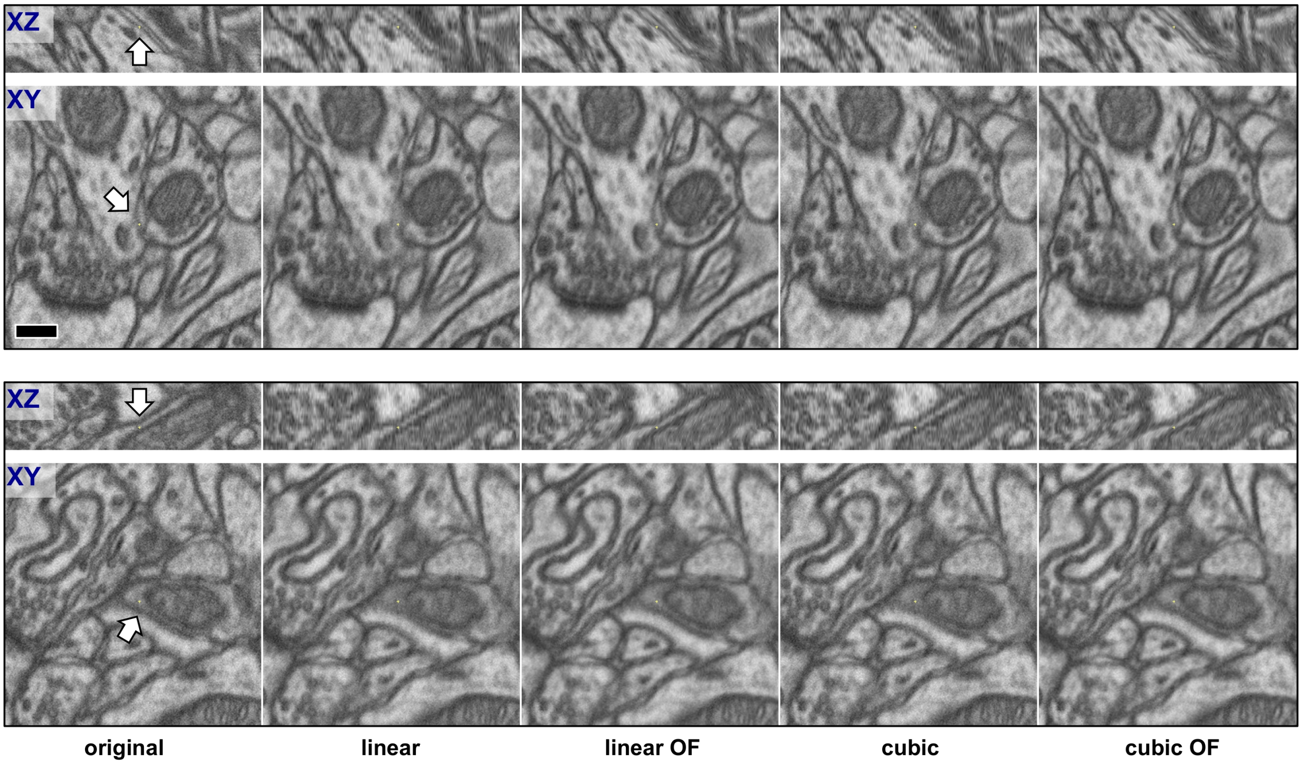

Figure 6: Isotropic stacks interpolated from the EPFL dataset under $\alpha = 4$ anisotropy condition. The leftmost column shows the original stack whereas the other columns present the results from the different methods. Two selected areas of the stack are presented at the top and bottom rows. In all cases, selected XY and XZ planes of the stacks are shown, whose correspondence is denoted by a small yellow point and arrows. The arrows also point to areas where the difference between the methods are noticeable. Bar: 200 nm.

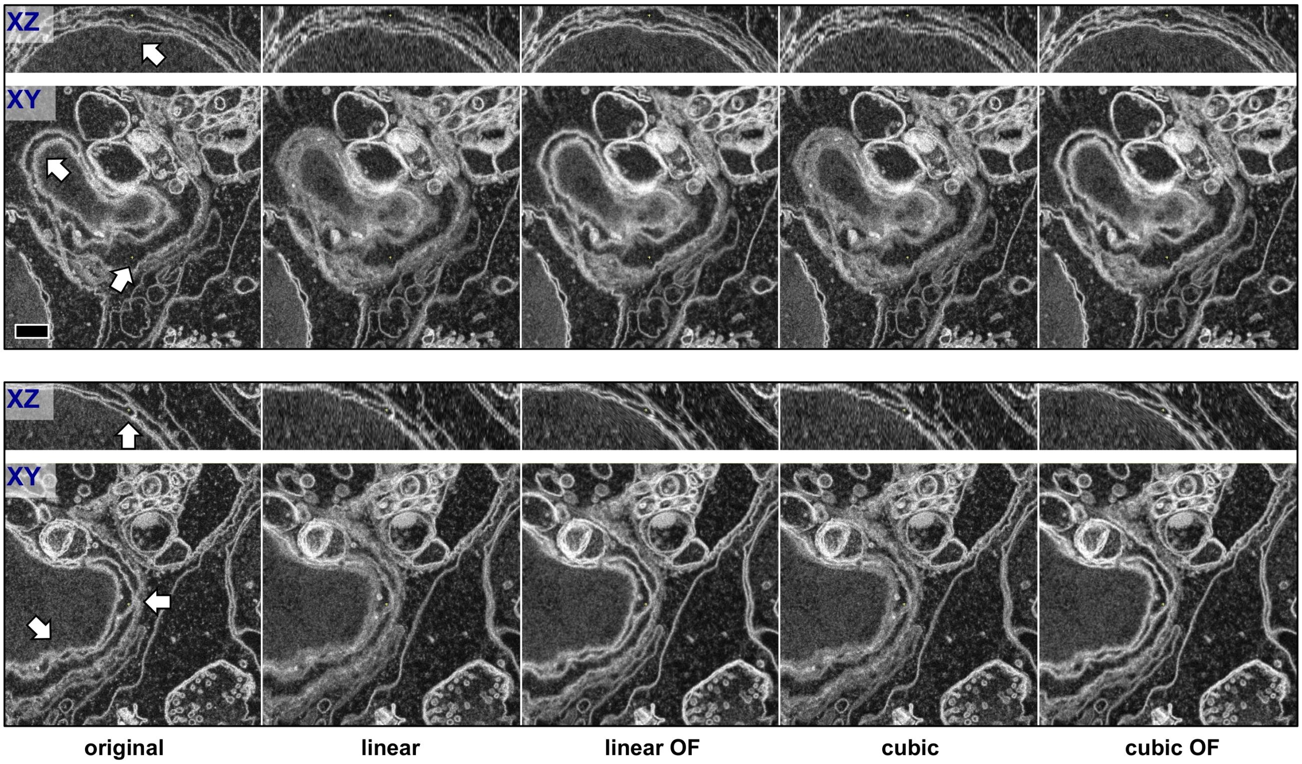

Figure 7: Isotropic stacks interpolated from the EMPIAR-10310 dataset under $\alpha = 4$ anisotropy condition. Two selected areas are presented (top and bottom rows) from the original stack (leftmost column) and from the interpolation methods. The presentation of the results follows the same convention as in Fig. 6. Bar: 500 nm.

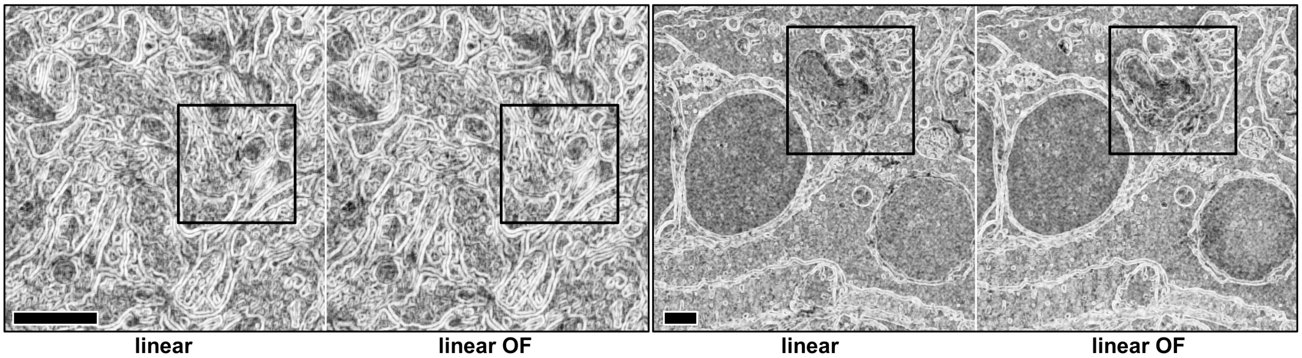

Figure 8: SSIM maps from EPFL and EMPIAR-10310 datasets. SSIM maps from images interpolated with linear and linear OF methods for both datasets (left and right, respectively) are shown. These images have indices 122 and 130 from the corresponding stacks, and their overall SSIM values are available in the curves presented in Figs. 4 and 5, respectively. Black squares mark the selected areas presented in Fig. 6(top) and Fig. 7(top), respectively. Bars: 1 μm.

3.2. Application to experimental anisotropic datasets

In order to evaluate the performance of the methods on an experimental dataset with an anisotropic resolution, we used a stack from human fibroblast cells acquired with a Zeiss Crossbeam 550 FIB-SEM microscope under cryogenic conditions using an image pixel size of 10.5 nm and a section thickness of 21 nm [10], which correspond to a step $\alpha = 2$. This dataset, publicly available at EMPIAR with ID 10515[4], is representative of the state-of-the-art FIB-SEM instruments, capable of working under cryogenic temperature to preserve the samples in near-physiological conditions. These data are characterized by a low signal-to-noise ratio and low contrast. The OF estimator was configured with the same parameters as in the previous section.

Figure 9 presents the effects of the interpolation methods with this dataset. As described previously, isotropic stacks were assembled by combining the experimental and the interpolated images. A specific area containing a mitochondrion (yellow point at the XY planes) close to the nucleus of a cell (bottom-right corner of the panels) is shown. The mitochondrion, as well as other nearby features, look blurred with classical interpolation (linear, cu-

---

[4] `https://www.ebi.ac.uk/empiar/EMPIAR-10515`

bic). In addition, the stair-like effects reported previously are also observable at the nucleus membrane in the XZ planes (indicated by an arrow). However, both OF-driven methods succeed in producing sharp interpolated images, as reflected in the well-defined mitochondrion and surrounding area. Figure 9 also confirms that linear OF and cubic OF behave similarly.

Figure 10 illustrates how linear OF outperforms the classical linear interpolation on another area of the stack around a mitochondrion. Top panels show two original experimental images serving as reference knots for the interpolation (denoted by αz and $\alpha(z+1)$). These images are 21 nm distant from each other. Biological structures may change importantly within this distance, as seen in the large mitochondrion in particular. As a result, the classical methods yield a blurred interpolated image (middle-left panel) whereas OF-driven ones manage to produce a sharp mitochondrion (middle-right) that represents an intermediate view between the reference knots. For illustration purposes, the displacement fields for the calculation of the linear OF result, as described in Section 2.4 and Figure 3, are shown at the bottom.

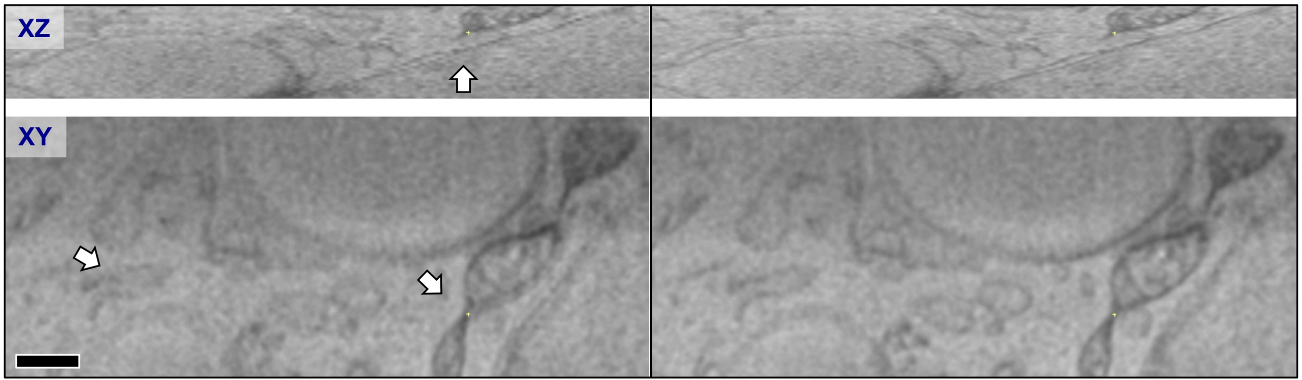

linear linear OF

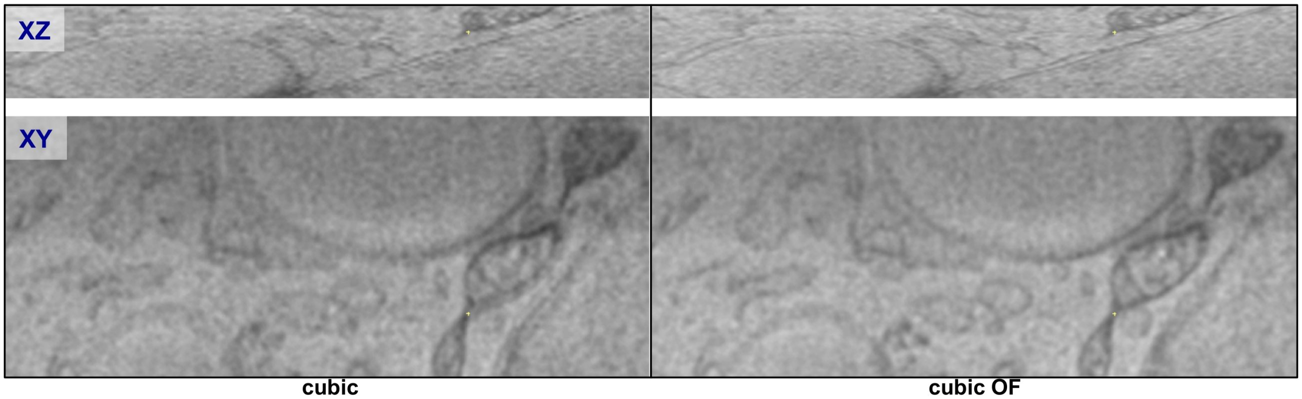

cubic cubic OF

Figure 9: Isotropic stacks interpolated from the EMPIAR-10515 dataset. This dataset was acquired under anisotropy conditions of $\alpha = 2$. Selected XY and XZ planes from an area of particular interest are presented, whose correspondence is denoted by a small yellow point and arrows. The arrows also point to areas with remarkable difference between the methods. Bar: 500 nm.

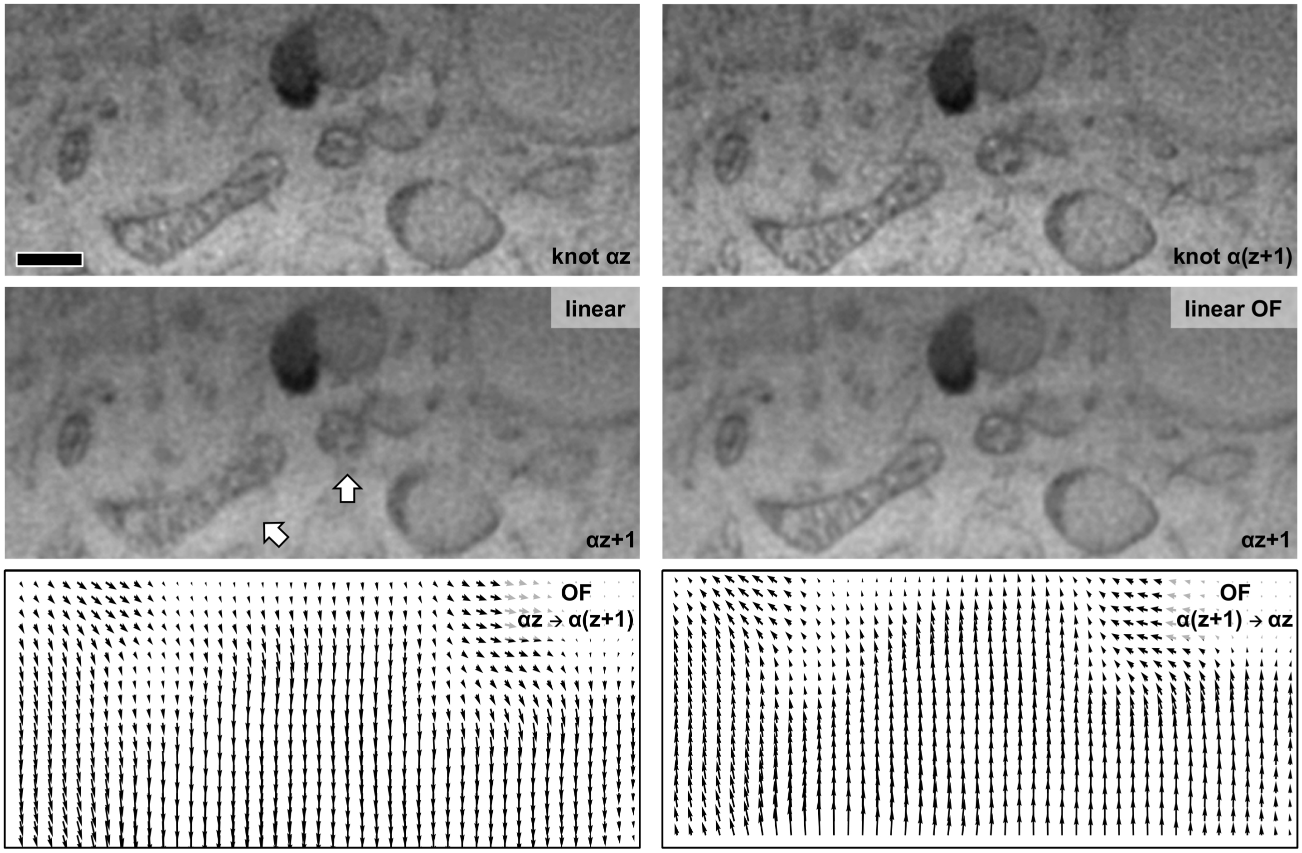

Figure 10: Interpolated images from the EMPIAR-10515 dataset. Top: two consecutive experimental images of the original stack acting as reference knots. Middle: results of the interpolation from the above two images with classical linear interpolation (left) and linear OF (right). Arrows point to two mitochondria (large and small) where the effects of the interpolation are dramatically different in linear OF. Bottom: Estimated displacement fields $\overset{\alpha z\to\alpha(z+1)}{\mathbf{d}}$ and $\overset{\alpha(z+1)\to\alpha z}{\mathbf{d}}$ (see Section 2.4 and Figure 3) involved in the calculation of the OF-compensated result (middle-right panel). Bar: 500 nm.

4. Discussion and Conclusion

In this work, we have presented an OF-driven interpolation approach to generating FIB-SEM stacks with isotropic resolution from experimental anisotropic data. Thanks to the OF, the interpolation adapts to the rapid variation of the biological structures observed through the images of the FIB-SEM stack, which is caused by their real 3D arrangement in the sample. The performance of our approach has been demonstrated with quantitative (in terms of SSIM) and qualitative evaluations. Our approach outperforms classical interpolation and manages to produce sharp interpolated views in cases where there are significant changes between consecutive experimental images. We have implemented and evaluated two strategies, OF-driven linear and OF-drive cubic, and found no remarkable differences between them.

The method works particularly well under the current acquisition protocols in FIB-SEM, involving an anisotropy of $\alpha = 2$ or $\alpha = 4$ (gaps between experimental images typically in the range of 10-20 nm), resulting in isotropic stacks with relatively homogeneous SSIM values. These results definitely support the use of anisotropic data acquisition protocols, which help reduce time, cost and system instabilities, complemented with OF-driven interpolation to yield isotropic FIB-SEM stacks. We also tested an extreme condition of $\alpha = 8$, which may resemble the experimental situations in Serial-Block-Face SEM (SBF-SEM), other type of large volume EM with gaps typically larger than 50 nm [1]. Although our method also outperforms classical interpolation in these extreme situations, the large SSIM oscillations of the resulting isotropic stacks suggest that the anisotropy may be excessive and that the gaps between the reference images are too large to be filled with homogeneous quality.

One important feature of our approach is the versatility to be applied straightforwardly to stacks of any origin. This is an important advantage since (a) the biological specimens being imaged with FIB-SEM, (b) the sample preparation techniques and (c) the image acquisition conditions may be highly diverse, as shown here with three representative datasets. In contrast, this fact may turn out to be a great disadvantage for recently proposed deep-learning-based methods because training for the specific target data would always be required [13, 14, 15].

Another advantageous attribute of our approach is its simplicity. The method has two main basic parameters associated to the OF estimator, namely the scale levels and the neighborhood window. They are related to the search area and the size of the biological structures of interest, respectively. The fact that these parameters are so well-defined facilitates their tuning for the specific study. In this work, we did not observe significant variation in the performance of the method with the parameters, though this may be certainly case-dependent. Our future plans include the development of strategies to optimize the OF parameters for the particular dataset under consideration. This optimization would open up the possibility of generating fine-tuned isotropic FIB-SEM stacks from anisotropic data in a fully automated fashion without user intervention.

Acknowledgements

This work has been partially supported by the Spanish Ministry of Science and Innovation/AEI (grants RTI2018-095993-B-I00 and SAF2017-84565-R), by the Spanish National Research Council (CSIC, grant 2020AEP029), by the European initiative Corbel (project id 2301), by the Junta de Andalucía (grants UAL18-TIC-A020020-B and P18-RT-1193) and by FEDER.

References

[1] C. J. Peddie, L. M. Collinson, Exploring the third dimension: Volume electron microscopy comes of age, Micron 61 (2014) 9–19. doi:10.1016/j.micron.2014.01.009.

[2] C. Kizilyaprak, Y.-D. Stierhof, B. M. Humbel, Volume microscopy in biology: FIB-SEM tomography, Tissue and Cell 57 (2019) 123–128. doi:10.1016/j.tice.2018.09.006.

[3] C. S. Xu, K. J. Hayworth, Z. Lu, P. Grob, A. M. Hassan, J. G. García-Cerdán, K. K. Niyogi, E. Nogales, R. J. Weinberg, H. F. Hess, Enhanced FIB-SEM systems for large-volume 3D imaging, eLife 6:e25916 (2017). doi:10.7554/eLife.25916.

[4] S. Saalfeld, R. Fetter, A. Cardona, P. Tomancak, Elastic volume reconstruction from series of ultra-thin microscopy sections, Nature Methods 9 (7) (2012) 717–720. doi:10.1038/nmeth.2072.

[5] D. P. Hoffman, G. Shtengel, C. S. Xu, K. R. Campbell, M. Freeman, L. Wang, D. E. Milkie, H. A. Pasolli, N. Iyer, J. A. Bogovic, D. R. Stabley, A. Shirinifard, S. Pang, D. Peale, K. Schaefer, W. Pomp, C.-L. Chang, J. Lippincott-Schwartz, T. Kirchhausen, D. J. Solecki, E. Betzig, H. F. Hess, Correlative three-dimensional super-resolution and block-face electron microscopy of whole vitreously frozen cells, Science 367:eaaz5357 (2020). doi:10.1126/science.aaz5357.

[6] A. Müller, D. Schmidt, C. S. Xu, S. Pang, J. V. D'Costa, S. Kretschmar, C. Münster, T. Kurth, F. Jug, M. Weigert, H. F. Hess, M. Solimena, 3D FIB-SEM reconstruction of microtubule–organelle interaction in whole primary mouse β cells, Journal of Cell Biology 220:e202010039 (2020). doi:10.1083/jcb.202010039.

[7] A. V. Weigel, C.-L. Chang, G. Shtengel, C. S. Xu, D. P. Hoffman, M. Freeman, N. Iyer, J. Aaron, S. Khuon, J. Bogovic, W. Qiu, H. F. Hess, J. Lippincott-Schwartz, ER-to-Golgi protein delivery through an interwoven, tubular network extending from ER, Cell 184 (2021) 2412–2429.e16. doi:10.1016/j.cell.2021.03.035.

[8] Y. Haridy, M. Osenberg, A. Hilger, I. Manke, D. Davesne, F. Witzmann, Bone metabolism and evolutionary origin of osteocytes: Novel application of FIB-SEM tomography, Science Advances 7 (14) (2021) eabb9113. doi:10.1126/sciadv.abb9113.

[9] M. Montero-Crespo, M. Domínguez-Álvaro, L. Alonso-Nanclares, J. DeFelipe, L. Blazquez-Llorca, Three-dimensional analysis of synaptic organization in the hippocampal CA1 field in Alzheimer's disease, Brain 144 (2) (2021) 553–573. doi:10.1093/brain/awaa406.

[10] Y. Zhu, D. Sun, A. Schertel, J. Ning, X. Fu, P. P. Gwo, A. M. Watson, L. C. Zanetti-Domingues, M. L. Martin-Fernandez, Z. Freyberg, P. Zhang, Serial cryoFIB/SEM reveals cytoarchitectural disruptions in Leigh Syndrome patient cells, Structure 29 (1) (2021) 82–87.e3. doi:10.1016/j.str.2020.10.003.

[11] A. M. Steyer, T. Ruhwedel, C. Nardis, H. B. Werner, K.-A. Nave, W. Möbius, Pathology of myelinated axons in the PLP-deficient mouse model of spastic paraplegia type 2 revealed by volume imaging using focused ion beam-scanning electron microscopy, Journal of Structural Biology 210 (2) (2020) 107492. doi:10.1016/j.jsb.2020.107492.

[12] R. M. Rudlaff, S. Kraemer, J. Marshman, J. D. Dvorin, Three-dimensional ultrastructure of Plasmodium falciparum throughout cytokinesis, PLOS Pathogens 16 (6) (2020) e1008587. doi:10.1371/journal.ppat.1008587.

[13] L. Heinrich, J. A. Bogovic, S. Saalfeld, Deep learning for isotropic super-resolution from non-isotropic 3D electron microscopy, in: M. Descoteaux, et al. (Eds.), MICCAI 2017, Lecture Notes in Computer Science, Vol. 10434, Springer, 2017, pp. 135–143. doi:10.1007/978-3-319-66185-8_16.

[14] K. Hagita, T. Higuchi, H. Jinnai, Super-resolution for asymmetric resolution of FIB-SEM 3D imaging using AI with deep learning, Scientific Reports 8:5877 (2018). doi:10.1038/s41598-018-24330-1.

[15] S. Deng, X. Fu, Z. Xiong, C. Chen, D. Liu, X. Chen, Q. Ling, F. Wu, Isotropic reconstruction of 3D EM images with unsupervised degradation learning, in: A. L. Martel, et al. (Eds.), MICCAI 2020, Lecture

Notes in Computer Science, Vol. 12265, Springer, 2020, pp. 163–173. doi:10.1007/978-3-030-59722-1_16.

[16] J. L. Barron, D. J. Fleet, S. S. Beauchemin, Performance of optical flow techniques, International Journal of Computer Vision 12 (1) (1994) 43–77. doi:10.1007/BF01420984.

[17] M. Nixon, A. Aguado, Feature Extraction and Image Processing for Computer Vision, Academic Press, 2019. doi:10.1016/C2011-0-06935-1.

[18] G. Farnebäck, Two-Frame Motion Estimation Based on Polynomial Expansion, in: Scandinavian conference on Image analysis, Springer, 2003, pp. 363–370. doi:10.1007/3-540-45103-X_50.

[19] H. Knutsson, C.-F. Westin, Normalized and Differential Convolution, in: Proceedings of IEEE Conference on Computer Vision and Pattern Recognition, IEEE, 1993, pp. 515–523. doi:10.1109/CVPR.1993.341081.

[20] P. Burt, E. Adelson, The Laplacian Pyramid as a Compact Image Code, IEEE Transactions on Communications 31 (4) (1983) 532–540. doi:10.1109/TCOM.1983.1095851.

[21] E. Catmull, R. Rom, A Class of Local Interpolating Splines, in: Computer aided geometric design, Elsevier, 1974, pp. 317–326. doi:10.1016/B978-0-12-079050-0.50020-5.

[22] P. Thévenaz, T. Blu, M. Unser, Interpolation Revisited, IEEE Transactions on medical imaging 19 (7) (2000) 739–758. doi:10.1109/42.875199.

[23] W. Burger, M. J. Burge, Digital Image Processing: An Algorithmic Introduction Using Java, Springer, 2016. doi:10.1007/978-1-4471-6684-9.

[24] B. Lucas, T. Kanade, An Iterative Image Registration Technique with an Application to Stereo Vision, in: Proceedings of the 7th international Joint conference on Artificial intelligence, 1981, pp. 674—-679. doi:10.5555/1623264.1623280.

[25] J. Wulff, M. J. Black, Efficient Sparse-to-Dense Optical Flow Estimation Using a Learned Basis and Layers, in: Proceedings of the IEEE Conference on Computer Vision and Pattern Recognition (CVPR), 2015, pp. 120–130. doi:10.1109/CVPR.2015.7298607.

[26] G. Knott, S. Rosset, M. Cantoni, Focussed Ion Beam Milling and Scanning Electron Microscopy of Brain Tissue, JoVE (Journal of Visualized Experiments) 53 (2011) e2588. doi:10.3791/2588.

[27] A. Lucchi, Y. Li, P. Fua, Learning for structured prediction using approximate subgradient descent with working sets, in: 2013 IEEE Conference on Computer Vision and Pattern Recognition, 2013, pp. 1987–1994. doi:10.1109/CVPR.2013.259.

[28] J. Hennies, J. M. S. Lleti, N. L. Schieber, R. M. Templin, A. M. Steyer, Y. Schwab, AMST: Alignment to Median Smoothed Template for Focused Ion Beam Scanning Electron Microscopy Image Stacks, Scientific Reports 10 (2020) 2004. doi:10.1038/s41598-020-58736-7.

[29] A. Iudin, P. K. Korir, J. Salavert-Torres, G. J. Kleywegt, A. Patwardhan, EMPIAR: A public archive for raw electron microscopy image data, Nature Methods 13 (2016) 387–388. doi:10.1038/nmeth.3806.

[30] Z. Wang, A. C. Bovik, H. R. Sheikh, E. P. Simoncelli, Image quality assessment: From error visibility to structural similarity, IEEE Transactions on Image Processing 13 (4) (2004) 600–612. doi:10.1109/TIP.2003.819861.